13 Computer Assisted Physics

P. F. Meier, R. M. Dünki, R. Füchslin, P. Gravila, P. Hüsser, S. Schafroth, and J. M. Singer

13.1 Introduction

The Computer Assisted Physics group has continued its research activities in computational physics. Selected examples of progress are presented in the following subsections. They comprise (i) simulations of superconducting tunneling junctions which are being developed at PSI as high resolution photon detectors and (ii) investigations of high-temperature superconductity, in particular cross-over, scaling and quantum critical phenomena. Quantum Monte Carlo simulations were performed to study the phase diagram of the attractive Hubbard model and the occurrence of the so-called spin gap. In addition, (iii) in a collaboration with the Institute for Physical Chemistry calculations for the polymerization of free radicals have been carried out. In a thesis work, the adsorbtion geometry of Na and K on the Si(001) surface has been calculated by means of density-functional methods (iv). Finally, (v) we report on the activities in the analysis of non–linear dynamical systems and biosignals, a project which is pursued in the frame of a collaboration with medical scientists.

13.2 Theoretical study of superconducting tunneling junctions

A photon hitting a superconductor produces quasiparticles and phonons. In a thin superconducting film these quasiparticles can be collected via a tunnel junction, and measuring their number allows to draw conclusions about the energy of the impacting photon. This detector scheme is far from being new, for semiconductors it is well known. Superconductors are of interest as detector materials because the gap energy of a superconductor is about thousand times smaller than that of semiconductor. The same photon energy produces more quasiparticles and therefore allows a higher resolution ($\approx 1/\sqrt{1000}$).

Recent developments in the production of superconducting tunneling junction detectors (STJD) focussed on thin, strip-shaped devices with two junctions (see fig. 13.1), one at each end. They allow in addition to the determination of the energy of the incoming photon a measurement of the position of the impact by comparing the energies collected by each of the junctions.

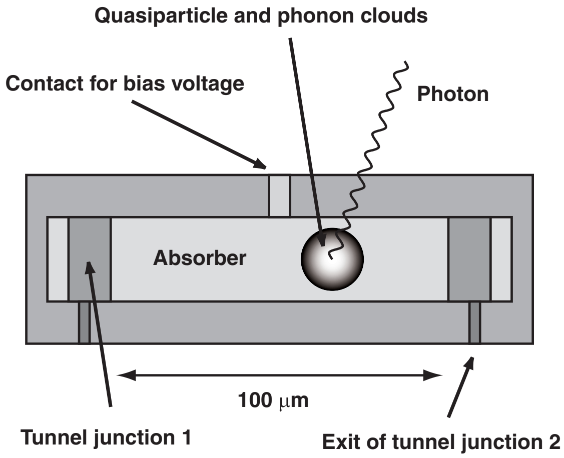

Figure 13.1: Scheme of a detector with two junctions.

In order to simulate the measured signal (the tunnel current in the junctions), one has to understand the dynamics of a STJD, which is governed mainly be two processes: First, the interaction of quasiparticles with phonons, which are described by a model of Chang and Scalapino. Second, diffusion takes place. We show that under certain circumstances the relaxation due to interactions and the diffusion can be decoupled.

The numerical solution of the Chang - Scalapino equations (CSE) is far from being trivial. It turned out that a direct approach by transforming the CSE, which are a system of integro-differential equations, into a system of ordinary differential equations does not always lead to satisfactory results. The amount of CPU - time needed is very high and occuring numerical problems cannot be neglected. Therefore, we were forced to develop an alternative procedure. By introducing a novel method of calculating specific numerical solution of integro-differential equations, which we call "pseudolinearization", and deriving an also novel method to calculate numerical integrals of a type typically occurring in scattering problems, we were able to overcome these difficulties. We showed that

- the quasiparticle and phonon distribution reach a quasistable state (a state which can be regarded as stationary with respect to time intervals of the order of microseconds) within a material and temperature dependent relaxation time τ_{relax},
- these distributions do not depend on the detailed structure of the initial distributions, but only on the energy of the impacting photon,
- after τ_{relax} and for temperatures below 1/4 T_c most of the energy is stored in the quasiparticle system.

The last fact is especially important because the operating temperature of a STJD is around 0.5 K and, as can be seen in fig. 13.2, materials like tantalum or niobium, which are favored as detector materials also for other reasons, exhibit a practically ideal efficiency.

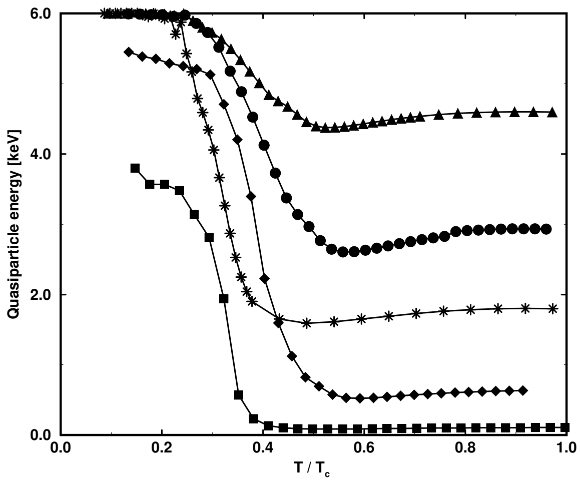

Figure 13.2: Energy of the quasistable quasiparticle distribution as a function of temperature after the impact of a 6keV photon. Ta: (●), Va: (▲), Sn: (♦), In: (■), Nb: ($*$).

We could also show that in the investigated systems the diffusion can be decoupled from the relaxation due to quasiparticle-phonon interactions. This fact allows to construct an efficient method to simulate the behavior of an STJD under inclusion of technical details of the measurement apparatus. Together with these simulations, an involved data analysis procedure could be set up and unknown parameters of the STJD could be calculated. In collaboration with A. Zehnder and his group at the PSI in Villigen, we were able to determine values for the diffusion constant of the quasiparticles and their effective lifetime.

The comparison of our calculations with recent experimental results [1, 2, 3] shows a good agreement. For special cases, theoretical investigations have been carried out by other authors (see for example Kaplan *et al.* [4]). Our results are fully compatible with their calculations. Therefore, we are convinced of the validity of our approach.

13.3 Crossover, scaling and quantum critical phenomena in high-temperature superconductors

We investigate crossover phenomena, universal scaling and quantum critical properties of high-temperature superconductors within three approaches:

13.3.1 Attractive Hubbard model

The first approach is the exploration of the phase diagram of the attractive Hubbard model by numerical quantum Monte Carlo methods as well as the scaling theory of quantum critical phenomena and approximative approaches. The attractive Hubbard model serves as a basic minimal model to give the proper (in view of the cuprates) phase transition phenomenology. We do not propose this model as a realistic high-T_c model itself, but use it to deepen our understanding of the phase diagram and to explore the effects of pairing fluctuations on various thermodynamic properties (density of states, spin susceptibility, etc.). Indeed, from the

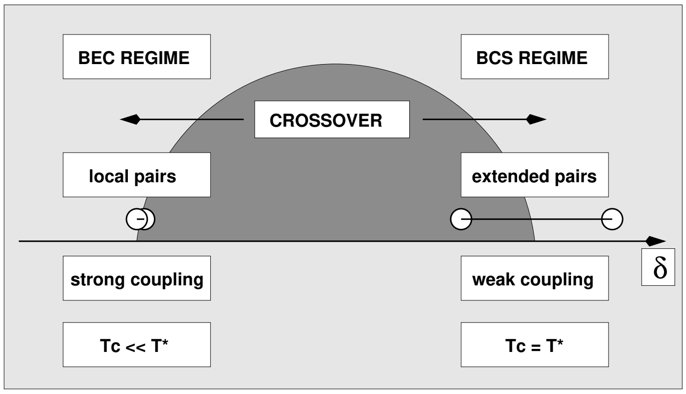

Figure 13.3: "Crossover" from a BCS-like endpoint to a BEC endpoint along the superconducting phase transition line. δ symbolizes a control parameter driving the crossover, which is in this phase diagram associated with the (inverse) coupling strength in case of the attractive Hubbard model and the electronic carrier doping in case of the cuprates.

aspect of universality and critical phenomena our analysis strongly reveals close similarities between the overdoped regime in the cuprates and the weak coupling regime of the attractive Hubbard model (both are close to a superconductor – normal metal endpoint) on the one side, and the underdoped respectively strong coupling regime (which are close to a superconductor to insulator critical endpoint) on the other side. Because of its conceptual simplicity, the attracive Hubbard model allows an easy investigation of the crossover from weak to strong coupling, from extended to local pairs, from BCS-like superconductivity to a Bose-Einstein condensation (BEC) of local pairs, just by tuning the coupling strength U, which acts as a control parameter for the phase transition line in analogy to the carrier doping in case of the cuprates.

13.3.2 Crossover and quantum critical properties in the cuprates

We apply the scaling theory of quantum phase transitions to the experimental phase diagram of high temperature superconductors in the temperature - doping plane. We find that the relation between transition temperature T_c and zero temperature penetration depth, and the sheet resistance become universal in the underdoped limit where the materials are essentially twodimensional and the insulator to superconductor transition occurs. The predominance of phase fluctuations in this doping regime manifests itself as a suppression of the fermionic density of states around the chemical potential, that is, in terms of a pseudogap. This provides a natural explanation of a variety of measurements, which show a pseudogap opening above T_c.

13.3.3 Universality and scaling theory of classical critical phenomena at finite temperature

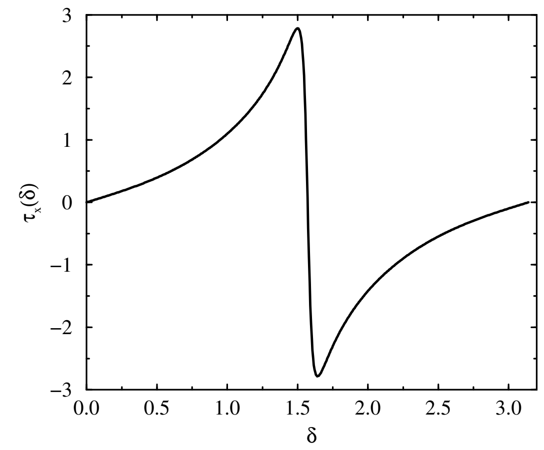

Figure 13.4: Theoretical prediction for the angular dependence of the magnetic torque τ_x for an anisotropic type-II superconductor with effective mass anisotropy $\gamma = 25$ in a regime close to but below T_c. This predictions are consistent with experimental data.

An anisotropic Ginzburg-Landau functional is used for extreme type-II superconductors such as the high-T_c cuprates in the presence of a magnetic field. This allows a formulation of the scaling properties for the singular part of the free energy. We can determine the limiting behavior of the scaling function in the vicinity of the zero-field transition temperature (where critical fluctuations dominate) from the existence of magnetization, a diamagnetic susceptibility and the Meissner effect. This allows predictions for the temperature and field dependence of a variety of quantities, among which angular dependence of the magnetic torque (which results from the noncollinearity of the magntic moment and field) in the superconducting state is shown.

The presented work has been carried out in collaboration with T. Schneider (Uni Zürich), M. Pedersen (U. Geneva), the Zurich University Magnetic Torque group (Prof. Keller and collaborators) and the Zurich University NMR group (Prof. Brinkmann and collaborators).

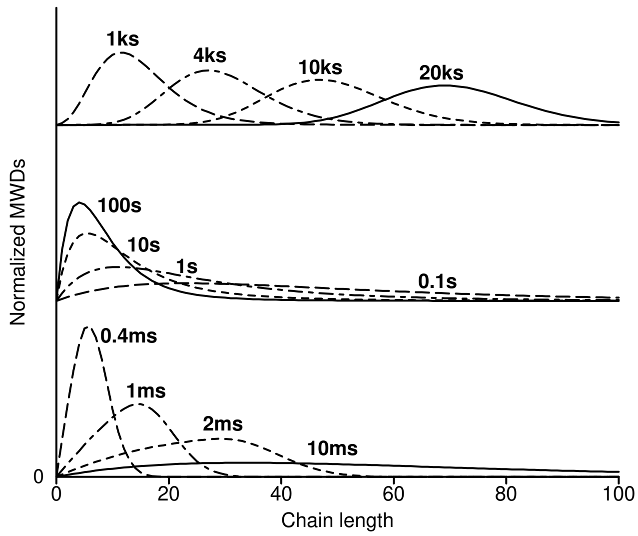

Figure 13.5: Time evolution of the molecular weight distribution (MWD). Traces are grouped and shifted vertically for clearness. Each trace is labeled with the corresponding time.

13.4 "Living" free–radical polymerization

"Living" free–radical polymerization (LFRP) has recently attracted much attention because it may avoid the shortcomings of conventional free-radical polymerization, in which broad polydisperse products are inherently produced. Polymers prepared using LFRP have some very desirable properties, namely low polydispersities and controllable molecular weight.

A model of such a LFRP scheme consists of the following reactions: activation/deactivation exchange between growing and dormant chains, chain propagation and an irreversible chain termination. The dormant chains are formed by a stable free radical and a growing chain. It is evident that the possibility of biradical termination to form dead polymers (polymers which do not react further) will be greatly reduced because of the equilibrium between the growing chain radicals and the stable radicals.

We started a collaboration with the physical chemistry institute to investigate the behavior of the LFRP scheme by a numerical model. The kinetics of the system can be modelled by a set of ordinary first order differential equations. By large-scale numerical simulations we got a more detailed understanding of the mechanisms of LFRP than is possible by analytical studies.

Some typical MWDs (molecular weight distributions) are shown in figure 13.5. For very small times, when the concentration of the stable radical is low, the chain growth is not controlled and the width of the MWD gets very large. At about 10 ms the width reaches a maximum. At this time the controlled chain growth starts. A peak in the MWD for small chain lengths begins to develop and shifts towards longer chain lengths as time and monomer conversion proceed. A monomer conversion of 90% is reached in about 12 hours. At that time the polydispersity index is 1.022 which is very close to the theoretical limit of one. The standard deviation of the MWD is 27 for a mean chain length of 200.

13.5 Theoretical determination of the adsorption geometry of Na on the Si(001) surface

The adsorption of metals on the Si(001) surface is a topic of great interest due to its scientific and technological importance. Many experimental techniques have been developed for investigating surfaces but, unfortunately, there is no single tool for measuring surfaces that has the reliability of X-ray crystallography for bulk. Usually, one has to postulate a surface structure in order to interpret the experimental data. On the other hand, density functional methods became increasingly successful in performing theoretical, *ab initio* calculations for surfaces.

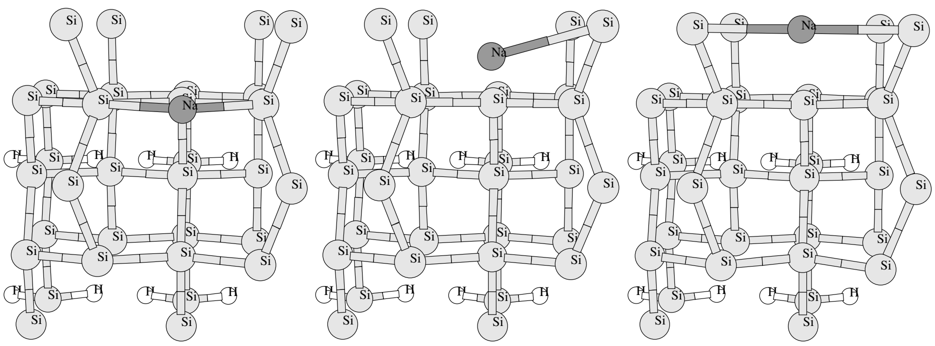

Figure 13.6: Transition of a Na adsorbate from the hollow to the cave site. Top view of the relaxation of the Na/Si(001) surface at a coverage of 1/4. The Na atom in the hollow site moves into the cave site. The starting position, an intermediate frame and the final position in the cave site are displayed.

From all metals, alkali metals such as Na and K are the simplest and the system Na (or K) on Si(001) became a benchmark for combined theoretical and experimental investigations. Many aspects of this surface like adsorption geometry, charge transfer, critical coverage are still debated.

We performed *ab initio* total-energy calculations for Na and K on the Si(001) 2×1 surface at coverages ranging from one-forth to one monolayer by the use of the density-functional method with a plane-wave basis set and a slab with a 2×2 surface cell.

In the initial stages of the energy optimization the Na approaches the surface with a simultaneous relaxation of the substrate atoms. Such a relaxation process is shown in Fig. 13.6. The adsorption of a Na atom in the "hollow" site (atop a Si atom of the third layer) turns out to be instable and the adsorbate moves into the "cave" site (atop a Si atom from the fourth Si layer). The forces acting on the ions are derived from the Hellmann-Feynman theorem. While for the electronic system a full quantum mechanical calculation is performed, the ions are relaxed using a classical Newton dynamics.

We obtained a highest coverage of one monolayer (i.e. two adsorbates per Si-Si dimer) corresponding to a double-layer structure with combined occupation of the hollow and pedestal sites. Thus, in the frame of our 2×2 surface cell, we predict an adsorption scenario with a phase transition during which adsorbates are moving from "cave" to "hollow" sites with increasing coverage.

We investigated the problem of the charge transfer between the alkali metal and the substrate using the difference between a converged density with a Na (or K) adsorbate and a similar slab with a clean Si(001) surface. Both alkali metals displayed a charge distribution pattern at 1/4 coverage that suggests a polarized covalent bond.

13.6 Dynamical systems analysis and biosignals

Our collaboration with the Cantonal Psychiatric Clinic in Rheinau continued. The aim is to explore the extent to which analysis of bio-medical time series by means of nonlinear dynamical systems theory improves current findings. In particular, we analysed the EEG of two groups, namely, 15 patients in the acute schizophrenic state and 15 controls in a healthy state. Both groups where exposed to different mental situations and each such situation resulted in three 30 second segments of EEG to be further analysed.
EEG were recorded according to the international 10-20 standard, which allows for the so-called parallel embedding scheme (Fig. 13.7).

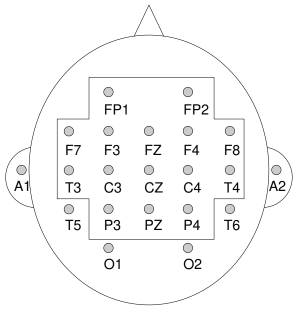

Figure 13.7: EEG-Electrode positions according to the international 10-20 scheme [7]. The measurements of the 15 electrodes from within the rectangle are included into the analysis, thereby building a 15 dimensional phase space.

One hereby regards each electrode as a coordinate in a phase space and includes the simultaneous time series from more and more electrodes in the analysis [5].
Our nonlinear EEG analysis follows a biparametric dimensional technique. In contrast to standard methods, this technique also considers attractor unfolding and the outcomes are several nonlinear measures, namely, the asymptotic correlation dimension (D_2), the so-called unfolding dimension m^* and the relative unfolding χ [6]. In addition, EEG analysis with conventional FFT techniques was performed at the hospital and clinical staff ranked each patient's symptoms on a psychiatric rating scale. First assessments using multivariate statistical techniques indicated significant differences in the EEG of patients and controls. This resulted in constructing a discriminance function which allows to correctly classify 83 % of the probands based on their EEG.

Deeper insight may be gained when relating the outcomes of our nonlinear EEG analysis with clinical measures. An example is shown in Fig. 13.8. The extrapolation of the regression line to symptom rating zero (where healthy probands are expected to reside) displays an interesting finding: This extrapolation does not match with the outcome of the healthy probands. Provided that there are no cumbersome effects due to distortion of the rating instrument, one may hypothesize that the psychotic state with no symptoms present does not imply the healthy state, which may point to the existence of a genuine transition between the two states.

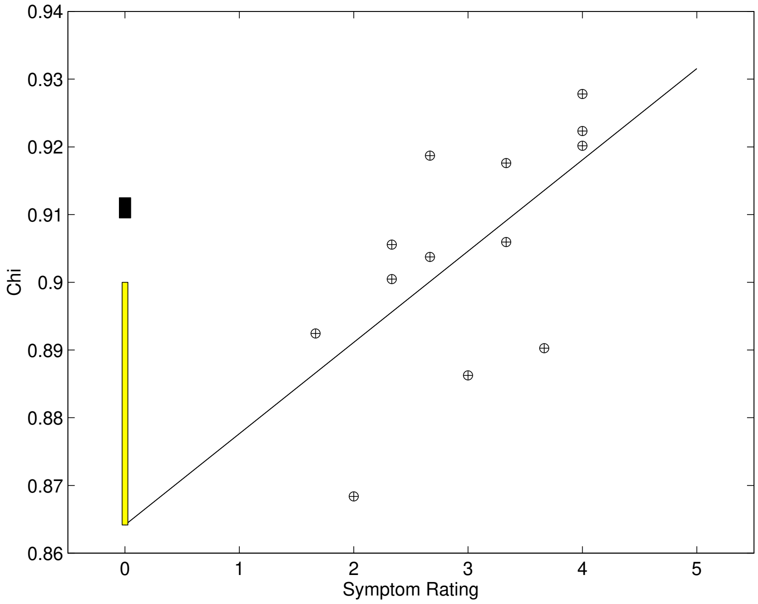

Figure 13.8: An example of symptom rating vs. EEG outcome. The extrapolation to rating zero along the regression line does not meet the average of the healthy probands (black rectangle). This is indicated by the 95% confidence interval (grey bar) for the regression line at this zero point.

References

[1] A. Zehnder, Phys. Rev. B 52, 12858 (1995).

[2] T. Nussbaumer, DISS. ETH, to be published (1998).

[3] K. Segall *et al.*, in the proceedings of LTD7, p. 47, (1997).

[4] S. B. Kaplan et al., Phys. Rev. B 14, p. 4854 (1976).

[5] R.M. Dünki and G.B. Schmid. Unfolding dimension and the search for functional markers in the human electroencephalogram. *Physical Review E*, 57:2115 – 2122, 1998.

[6] G.B. Schmid and R.M. Dünki. Indications of nonlinearity, intraindividual specifity and stability of human EEG: The unfolding dimension. *Physica D*, 93:163 – 190, 1996.

[7] H.H. Jaspers. The ten-twenty electrode system of the international federation. *Electroencephal. Clin. Neurophysiol.*, 10:371 – 375, 1958.